



Multiphase distribution in partly saturated hierarchical nonwoven fibre networks under applied load using X-ray computed tomography

Patrick Wegele^{1,2} · Tomas Rosén¹ · Daniel Söderberg¹

Received: 10 July 2024 / Revised: 1 August 2024 / Accepted: 7 August 2024
© The Author(s) 2024

Abstract

In many industrial applications, nonwoven fibre networks are facilitated to operate under partly saturated conditions, allowing for filtration, liquid absorption and liquid transport. Resolving the governing liquid distribution in loaded polyamide-6 (PA6) fibre networks using X-ray computed micro-tomography is a challenge due to the similar X-ray attenuation coefficients of water and PA6 and limitations in using background subtraction techniques if the network is deformed, which will be the case if subjected to compression. In this work, we developed a method using a potassium iodide solution in water to enhance the liquid's attenuation coefficient without modifying the water's rheological properties. Therefore, we studied the evolving liquid distribution in loaded and partly saturated PA6 fibre networks on the microscale. Increasing the external load applied to the network, we observed an exponential decrease in air content while the liquid content was constant, increasing the overall saturation with increasing network strain. Furthermore, the microstructural properties created by the punch-needle process in the manufacturing of the network significantly influenced the out-of-plane liquid distribution. The method has been proven helpful in understanding the results of adaptations in both the fibre network design and manufacturing process, allowing for investigating the resulting liquid distribution on a microscale.

1 Introduction

In numerous practical applications such as filters, repellent textiles, composite manufacturing, or pulp moulding, the liquid distribution within the fibre network governs the overall product or process performance. It is essential when using nonwoven structures, which often show pronounced anisotropic liquid transport properties. This is a consequence of their internal structure, which can be influenced by the engineering and manufacturing process of the nonwovens. Hence, there is a clear need to understand the impact of

the nonwoven design and manufacturing processes on the resulting liquid distribution within these networks.

The liquid penetration length L within a partly saturated porous medium can be described by the Lucas–Washburn equation (Washburn 1921) using the liquid surface tension γ_{lg} , the pore radius r , the solid–liquid contact angle θ_{sl} and the viscosity η :

$$L = \sqrt{\frac{2\gamma_{lg} r t \cos \theta_{sl}}{4\eta}} \quad (1)$$

After infinite time t , a certain liquid distribution is established that is governed by an equilibrium of the capillary pressure and hydrostatic pressure, taking into consideration the density ρ and the height h :

$$\frac{2\gamma_{lg} \cos \theta_{sl}}{r} = \rho g h \quad (2)$$

Furthermore, the overall structure and pore size distribution of porous medium will govern the accessibility of pores with radius r , which further affects the final liquid distribution in the partly saturated case.

Much work has already been done to understand the liquid distribution in fibre systems. For woven networks,

✉ Daniel Söderberg
dansod@kth.se

Patrick Wegele
pwege@kth.se

Tomas Rosén
trosen@kth.se

¹ Department of Fibre and Polymer Technology, KTH Royal Institute of Technology, Teknikringen 56, 10044 Stockholm, Sweden

² J.M. Voith SE & Co. KG, St. Poeltener Strasse 43, 89522 Heidenheim an der Brenz, Germany

the structure (Birrfeider et al. 2013; Hollies et al. 1957; Yousefi et al. 2021; Zhang et al. 2017) and solid–liquid contact angle between the fibres and the liquid (Birrfeider et al. 2013; Biguenet et al. 2024) are key parameters that influence the liquid distribution in both the in-plane and out-of-plane direction. In these systems, external forces can increase the out-of-plane liquid transport (Rossi et al. 2011; Stämpfli et al. 2013) until a limit of void space is reached (Zhuang et al. 2002). Similar observations had been made for nonwoven networks, where the fibre orientation and pore size distribution determine the liquid distribution anisotropy (Mao and Russell 2003). As the liquid accumulates along the fibres in small pores in the top fibre layer, an inhomogeneous out-of-plane liquid distribution is often present, where local areas of absolute saturation can occur at small pores due to high capillary pressure (Charvet et al. 2011; Penner et al. 2021; Hoppe et al. 2022). These areas can supply liquid to neighbouring pores once external loads deform the network.

Determining the local liquid distribution in partly saturated fibre networks is complicated due to the small spatial scales of these networks. Even though numerical methods have been developed (Hyväluoma et al. 2006; Markicevic and Navaz 2009), these problems are usually investigated experimentally due to the complexity of the underlying structure. Besides visual investigations (Harnett and Mehta 1984), measurements of the electrical conductivity (Hu et al. 2005; Van Langenhove and Kiekens 2001), with scanning electron microscopes (SEM) (Zhang and Zhang 2022), serial sectioning-imaging (Jaganathan et al. 2009) and nuclear magnetic resonance (NMR), were utilized to resolve the liquid distribution in fibre networks (Bencsik et al. 2008; Endruweit et al. 2011; Leisen and Beckham 2001, 2008). As all these methods have some drawbacks regarding three-dimensional analysis, spatial resolution, necessity of full saturation or pore size assumption, X-ray-based methods are frequently used to visualize liquid within partly saturated fibre networks (Birrfeider et al. 2013; Charvet et al. 2011; Chaudhuri et al. 2022; Hoppe et al. 2022; Manke et al. 2007; Roels and Carmeliet 2006; Rossi et al. 2011; Straube et al. 2023; Weder et al. 2006). This method makes a distinction between liquid, fibres and air possible due to the different X-ray attenuation coefficients μ_i of the respective materials. The intensity I_i of a beam transmitted through a substrate with μ_i and the length l can be derived using Beer–Lambert’s law assuming a monochromatic beam and a single homogeneous material:

$$I_i = I_0 e^{-\int \mu_i dl} \quad (3)$$

In practice, achieving contrast between different materials can be difficult, as differences in μ_i will influence I_i as an

exponential decay, meaning that significant differences in μ_i are necessary to obtain sufficient differences in I_i for distinguishing between different materials.

One method to overcome this challenge is to obtain a dry scan and subtract the volumetric image from the volumetric image of the wet scan (e.g. (Chaudhuri et al. 2022; Eller et al. 2011; Stämpfli et al. 2013; Yamaguchi et al. 2021)). As a result, materials with similar μ_i , such as water and synthetic fibres, can be distinguished. However, this approach is impossible when external loads cause internal movements within the fibre structure. Furthermore, poor contrast between liquid and air can cause small liquid volumes in the range of 10 μm to not be resolvable (Yamaguchi et al. 2021). Another possibility for resolving such systems is the holotomography method (Charvet et al. 2011), which is only available at synchrotron beamlines.

Other studies rely on using contrast agents to increase the X-ray attenuation coefficient of the liquid by adding chemicals with components of high atomic number. For the particular case of fibre networks, several different contrast agents had been used like barium chloride (BaCl_2) (Gupta et al. 1997), meglumine ioxitalamate (Weder et al. 2006), potassium iodide (KI) (Hoppe et al. 2022; Halls et al. 2018), caesium iodide (CsI) (Wallmeier et al. 2021), barium sulphate (BaSO_4) (Davit et al. 2011), iron(II)-sulphate (FeSO_4) (Carrel et al. 2017), 1-chloronaphthalene ($\text{C}_{10}\text{H}_7\text{Cl}$) (Ivankovic et al. 2016), caesium chloride (CsCl) (Ferdoush et al. 2023), Fe_2CoO_4 (Hobisch et al. 2021) or even silver-coated nanoparticles (Iltis et al. 2011). However, staining the liquid with a contrast agent might alter the liquid properties and, therefore, affect the liquid distribution in the fibre network, which requires a careful choice of a suitable contrast agent.

As a result, much work has already been done to understand the principles of droplet penetration in multilayer fibre networks and their visualization. It usually results in inhomogeneous partly saturated networks, where the liquid accumulates in voids due to the governing capillary pressure. In numerous applications such as composite manufacturing and pulp moulding, these networks are subjected to external loads, removing air from the matrix. As this process governs the final product quality, we propose an X-ray computed tomography method to investigate the liquid distribution within partly saturated fibre networks under external loads. In our particular case, we focus on resolving the water distribution in hierarchical nonwoven polyamide-6 (PA6) fibre networks similar to the ones investigated by Thibault and Bloch (Thibault and Bloch 2002). This is a particular challenge due to the similar attenuation coefficients of water and PA6 (see Sect. 2.3).

2 Experimental

2.1 Experimental μ CT setup and X-ray parameters

The tomographic scans of the underlying study are recorded using a Pheonix Nanotom M nanofocus X-ray computer tomography system (GE Sensing & Inspection Technologies GmbH, Wunstorf) with an air-conditioned cabinet. It is equipped with a temperature-stabilized high-dynamic DXR detector, allowing a resolution of 3072×2400 pixels. Aluminium-molybdenum is used as a target material. The tomographic scans are recorded under a rotation of 360° of the sample holder, which is a tube manufactured from polymethylmethacrylate (PMMA), selected due to its low X-ray attenuation coefficient. As visible in Fig. 1, the application of external loads on the sample is possible using a PMMA piston, which is loaded before the scan and locked by a clamping set. This makes the process of load application considerably easier than in previous compression studies of nonwoven networks (Jaganathan et al. 2009). As the setup is not sealed towards the loading position, air and water pressed out of the sample at higher loads can escape without restrictions. The total scan time required for one scan at a voxel size of $6 \mu\text{m}$ was around 50 min, which also contains warm-up time and the recording of calibration images. Further parameters used for the μ CT scans can be found in Table 1.

In total, 1000 images were used for the tomographic reconstruction, which was achieved using an algorithm based on Feldkamp's cone beam reconstruction algorithm (Feldkamp et al. 1984). It leads to a stack of greyscale 2D

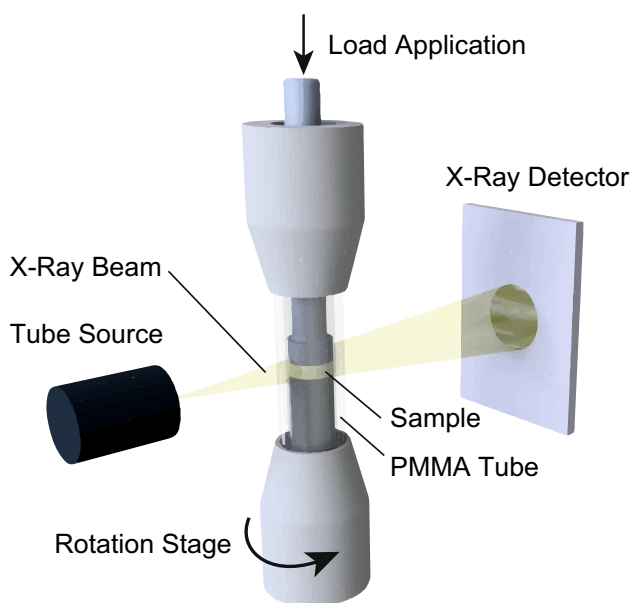


Fig. 1 Experimental setup used in the μ CT. The sample is placed in a PMMA sample holder, which allows additional loading with the top piston. The 360° rotation stage allows for X-ray imaging of all desired directions. The PMMA tube is not sealed against the sample, allowing for a radial flow of air and liquid

Table 1 Used equipment and parameters in the μ CT-scans

CT System	GE Phoenix Nanotom M
Detector type	DXR detector with 3072×2400 pixels
Filter	0.5 mm Aluminium
Target material	Aluminium Molybdenum target
Acceleration voltage	85 kV
Beam current	250 μA
Voxel size	$4 \mu\text{m} / 6 \mu\text{m}$
Scanning volume	$6 \times 6 \times 6 \text{ mm}$ (max.)
Images per rotation	1000
Scan time per image	1 s
Total scanning time	50 min

images of the scanned structure, which are post-processed using a despeckling filter. Afterwards, manual material segmentation using the greyscale histograms of the images should allow for distinguishing PA6 fibres, liquid, and air within the tomographic scan. This requires a sufficient X-ray contrast between the different phases, which will be considered in Sect. 2.3.

2.2 Micro-structural characterization of the network and dry analysis

A multilayer fibre network consisting of PA6 fibres is used in the underlying study. It consists of nonwoven batt fibre layers, which are mechanically attached by a needle punching process to a two-layered woven base layer consisting of multifilament yarns with a 0.2 mm fibre diameter. This process is schematically shown in Fig. 2a, where reciprocating barbed needles are used to mechanically entangle the nonwoven batt fibres into the woven base fibre layer to produce a fabric. These needles pull some batt fibres from the nonwoven top layer downwards, causing increased network cohesion. On the other hand, pillars of batt fibres orientated in the z-direction are formed due to the needle punch process (Russell 2022). Such needle-punched fabrics have numerous applications, including their usage as technical textiles, which require controlled permeability under load for drainage (Thibault and Bloch 2002; Thibault et al. 2001). In many practical cases, partly saturated conditions are present in these networks. As the liquid should be removed from the network efficiently under compression, it is of interest to investigate the evolving liquid distribution under external load and in which way the needle-punched network structure influences the liquid distribution. For investigation, we use a punch to cut out a round sample of $D = 10 \text{ mm}$ diameter from the fabric. The resulting specimen can be seen in Fig. 2b. For the first structure classification, a μ CT scan of the dry sample is obtained using beam parameters as listed in Table 1 with a

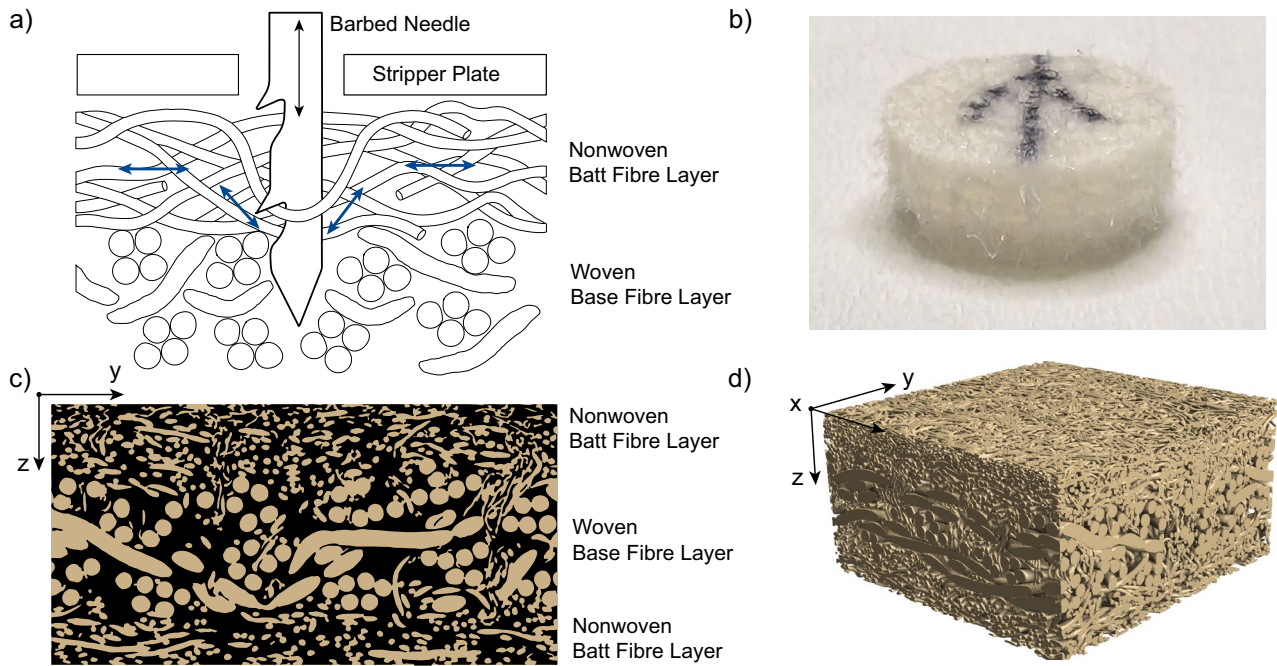


Fig. 2 Characterization of the dry fabric used in the underlying study using an X-ray computed tomographic scan. The parameters used for the scan are the same as listed in Table 1. **a** Scheme of the punch needle process where the nonwoven batt fibre layer is mechanically attached to the woven base fibre layer. The fibre direction of the batt

fibres is changed along the needling paths as indicated by the blue arrows. **b** $D = 10$ mm sample used for the tomographic investigation. **c** 2D material structure with the batt and base fibre layers visible. **d** Principal structure and shape of the 6x6 mm cuboid used for the investigation

voxel size of $6 \mu\text{m}$. Only the central area of 6x6 mm is used for further investigation, as depicted in Fig. 2d.

To evaluate the underlying structure, we calculate the solid and pore size distribution using a granulometry approach as described by Hilpert and Miller (2001) and implemented by Schulz et al. (2007). Within that approach, a morphological opening is used to calculate the part of a pore/solid space X in which a spherical structuring element B can be fit in:

$$O_B(X) = \cup\{B|B \subseteq X\} \quad (4)$$

In this operation, an erosion using the structuring element B of increasing radius r is applied first to determine the centre points x where a sphere can fit without touching the fibre/pore boundaries:

$$\varepsilon_{B_r}(X) = \{x : B_{x,r} \subseteq X\} \quad (5)$$

The eroded set is then dilated using the identical structuring element as in the initial operation:

$$D_{B_r}[\varepsilon_{B_r}(X)] = \{x : B_{x,r} \cap \varepsilon_{B_r}(X) \neq \emptyset\} \quad (6)$$

Hence, it is possible to determine the maximum diameter of spheres that can be fitted into the respective fibre voxels. Applying this method to the fibres in the fabric, one can

clearly distinguish between the nonwoven batt fibre layers and the woven base layer, as visible in Fig. 3a. A solid size diameter analysis in Fig. 3b allows quantifying the fibre diameter in the respective layers. The top batt layer is formed by thin fibres with a diameter of $32 \mu\text{m}$, followed by a more coarse second batt layer with a diameter of $66 \mu\text{m}$. These layers are punch-needled on a woven base layer of multifilament yarns with single fibre diameters of $195 \mu\text{m}$. Another batt fibre layer with $66 \mu\text{m}$ diameter fibres is used on the bottom side.

Besides the solid size distribution, the granulometry approach is applied to determine the pore size distribution, as depicted for a slice in the yz -plane in Fig. 3c. It can be seen that small pores are present within the first two batt layers. Within the woven base layer, the biggest pore sizes can be found due to the thick base fibre layer. Furthermore, the pillars created by the punch needle process are also visible as batt fibres whose principal orientation is along the z -axis, similar to the observation of Thibault and Bloch (2002). Consequently, locally small pore sizes are present in these pillars, even within the woven base layer. We can determine the relative pore volume distribution by calculating the relative volume of pores of specific diameter over the fabric thickness z . As visible in Fig. 3d, the majority of the small pores ($< 50 \mu\text{m}$ and $50\text{--}100 \mu\text{m}$) can

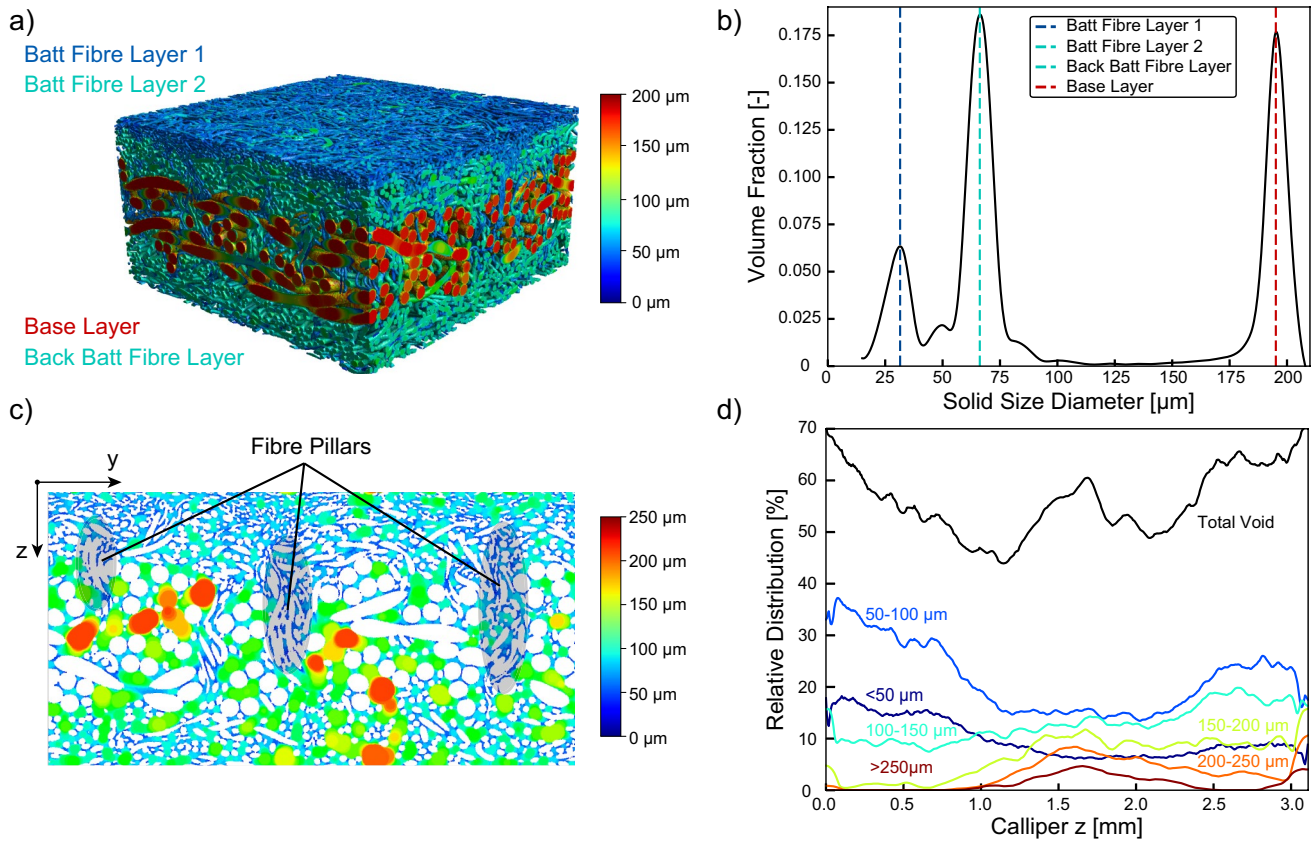


Fig. 3 Evaluation of the volumetric tomographic reconstruction. **a** Solid size analysis (granulometry) of the fibres from the tomographic scan of Fig. 2d. Fibres of different diameter D are coloured according to the determined diameter. Different nonwoven batt layers and woven base layers are clearly visible. **b** Volume fraction of the solid sizes within the network. Peaks at 32, 66 and 195 μm correspond to the

fibre diameters in the respective layer and can be expressed in the unit dtex. **c** Pore size analysis (granulometry) depicted in a slice of the yz -plane of the fabric. Fibre pillars resulting from the needle punching process are clearly visible. **d** Analysis of the pore size as a function of the z -direction

Table 2 Attenuation coefficient μ_i for different materials for the characteristic X-ray energies $L\alpha 1 = 2.293 \text{ keV}$ and $L\beta 1 = 2395 \text{ keV}$, calculated from Henke et al. (1993)

Material	Attenuation coefficient μ_i (1/m)	
	2.293 keV	2.394 keV
PA6	37,553	33,117
Water	42,326	37,449
Air	46	40
KI	104,418	94,036

Air is assumed to be a mixture of 78% N_2 , 21% O_2 and 1% Ar. Values for water assume solid-state. The attenuation coefficient is calculated as the reciprocal of the attenuation length

be found just below the upper surface until a depth of around 0.7 mm. Below this, a layer of bigger pores (150–200 μm , 200–250 μm , > 250 μm) is formed in the base layer, whereas in the back batt fibre layer, small- and medium-sized pores

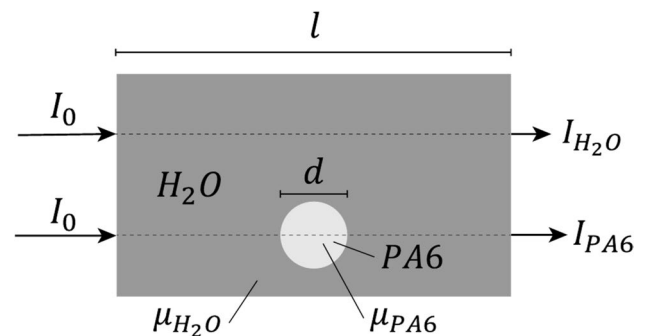


Fig. 4 The model assumption for calculating the differences in intensity of an X-ray beam of 2.293 keV will have after transmitting through a distance of l with or without a PA6 particle of the diameter d

(50–100 μm , 100–150 μm) are dominant. Finally, the overall relative porosity of the unloaded sample is calculated by voxel counting to $\phi_r = 55.51$.

2.3 Material segmentation in wet sample conditions

As we run the μ CT in the absorption contrast imaging mode, significant differences in the attenuation coefficients are necessary to distinguish different materials due to Beer–Lambert’s law (see Eq. 3). Besides the atomic number, the characteristic X-ray energy influences the resulting attenuation coefficients of the transmitted materials. Assuming a monochromatic X-ray beam resulting from an $L\alpha 1$ or $L\beta 1$ transition within a molybdenum atom, the characteristic X-ray energies are $L\alpha 1 = 2.293$ keV and $L\beta 1 = 2.395$ keV. Therefore, the resulting attenuation coefficients can be determined for PA6, water and air, as depicted in Table 2.

It is apparent that the similar attenuation coefficients of water and PA6 will cause similar X-ray intensities on the detector, making it challenging to distinguish between the materials in the greyscale tomography. For the underlying case, the relative differences in the intensity on the detector for a single batt fibre of $d = 16 \mu\text{m}$ in a system with a length of $l = 6$ cm, as shown in Fig. 4, can be calculated:

$$I_{\text{H}_2\text{O}} = I_0 e^{-\mu_{\text{H}_2\text{O}} l} \tag{7}$$

$$I_{\text{PA6}} = I_0 e^{-\mu_{\text{H}_2\text{O}}(l-d) - \mu_{\text{PA6}} d} \tag{8}$$

From that, the ratio $I_P/I_{\text{H}_2\text{O}}$ is determined to be 1.079, meaning that differences in intensity of only around 8% occur. To check the resulting differences in greyscale, we apply 20 μl of purified water to the sample described in Sect. 2.2 and record a tomographic scan. The resulting greyscale reconstruction can be seen in Fig. 5a. Even though one can spot water within the batt fibre layers due to the formation of closed surfaces, there is not enough greyscale contrast to perform a segmentation of PA6 and water. This is confirmed by looking at the greyscale histogram in Fig. 5b,

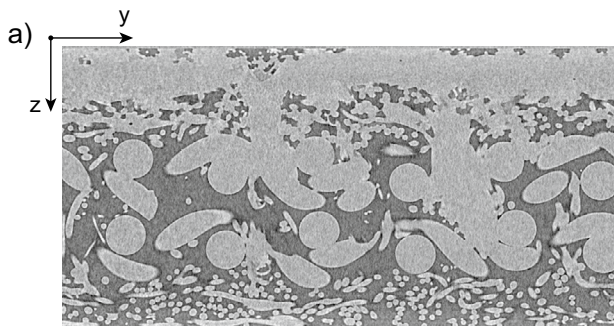


Fig. 5 **a** yz -plane greyscale image when 20 μl of purified water had been applied to a $D = 10$ mm sample and scanned in the μ CT. The total water saturation was determined to be 18%. **b** Corresponding

which does not allow a distinction between PA6 and water. Hence, the theoretically determined contrast differences of 8% are insufficient for the material distinction in a practical μ CT approach. This causes a need to stain the water with a contrast agent, which increases the attenuation coefficient of the liquid phase.

However, the static liquid distribution in fibre networks results from the equilibrium of the local capillary pressure and the hydrostatic pressure, as mentioned in Eq. 2. Therefore, an addition of contrast agents into the purified water must not considerably influence the liquid properties in terms of static contact angle θ_{sl} against PA6, liquid–gas surface tension γ_{lg} and density of the liquid ρ . This leads to the conclusion that studying realistic water distribution using contrast agents requires checking the liquid properties and comparing them with purified water.

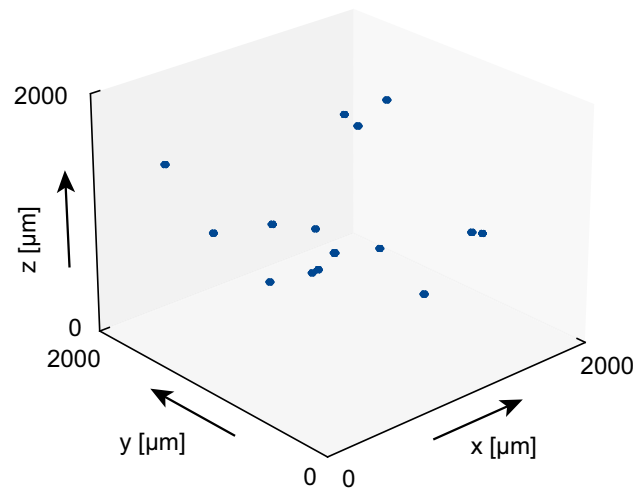
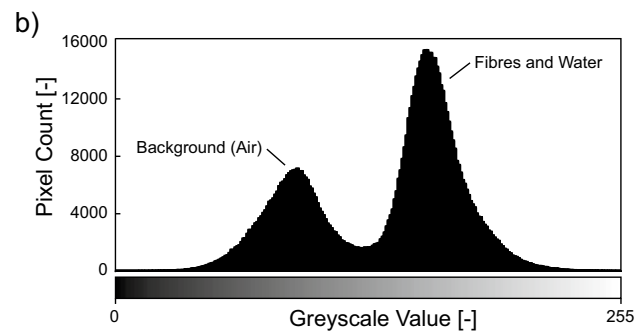


Fig. 6 Reference systems with $2 \times 2 \times 2$ mm volume and 15 randomly spaced PA6 particles of $16 \mu\text{m}$ size. For visualization, the size of the particles is magnified by factor 2



greyscale histogram. Peaks refer to the background (air) and to fibres and water. There is no possibility to distinguish between fibres and water by greyscale thresholding within the second peak

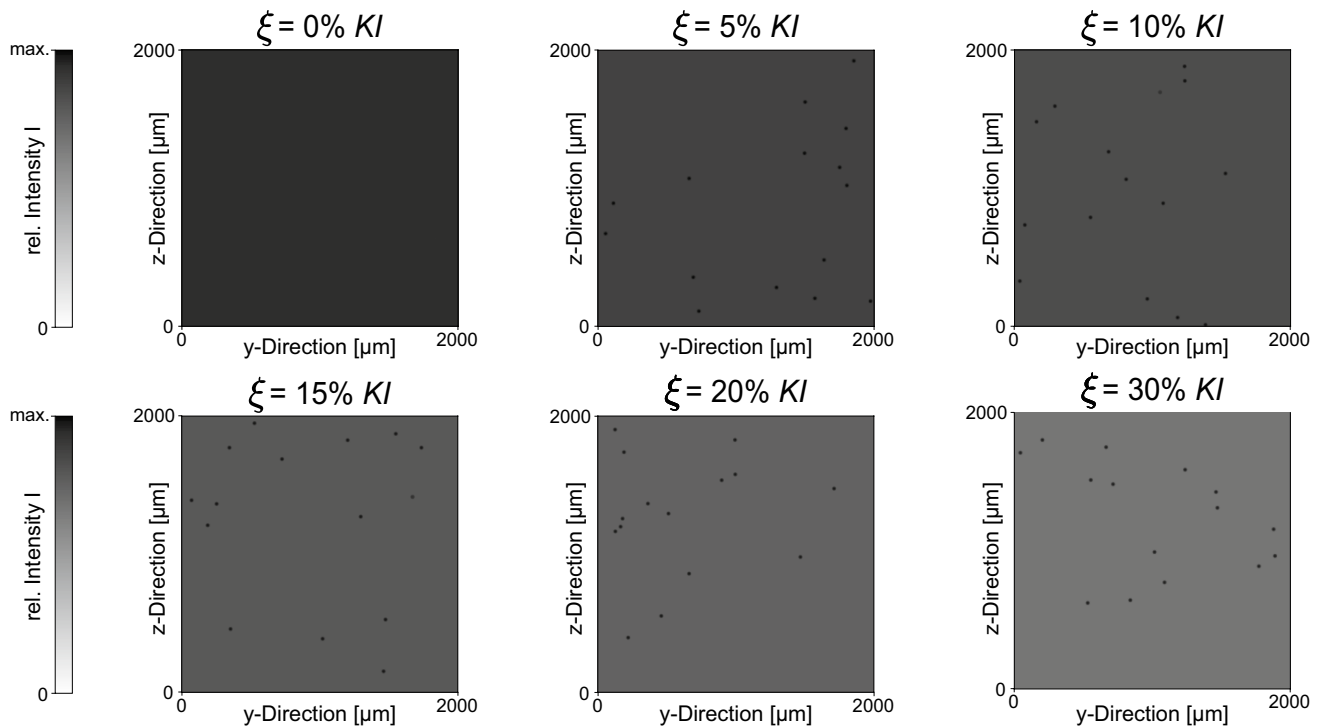


Fig. 7 Absorption contrast of randomly spaced PA6 particles in water with different concentrations of *KI* on a virtual detector in the *yz*-plane for an X-ray energy of 2.293 keV. The intensity of the beam

transmitting the centre of a particle is set as a maximum intensity threshold for the colourbar

2.4 Experimental study of contrast liquid

The X-ray attenuation coefficient of water can be significantly increased by staining it with elements of higher atomic number. As particles of potassium iodide (*KI*) provided good results (Hoppe et al. 2022), we are choosing different concentrations of potassium iodide mixed in purified water as a liquid for resolving it together with PA6 fibres within a tomographic scan. In contrast to other

possible additives, potassium iodide offers some advantages, like high solubility in water, good availability, and safe usage, which makes it a beneficial contrast agent.

To keep the amount of necessary μ CT scans low, we simulate the contrast between PA6 particles and different water and *KI* concentrations in a reference system. Therefore, we randomly place PA6 particles of 16 μ m diameter (according to the batt fibre diameter of the underlying network) in a cube of $2 \times 2 \times 2$ mm. This

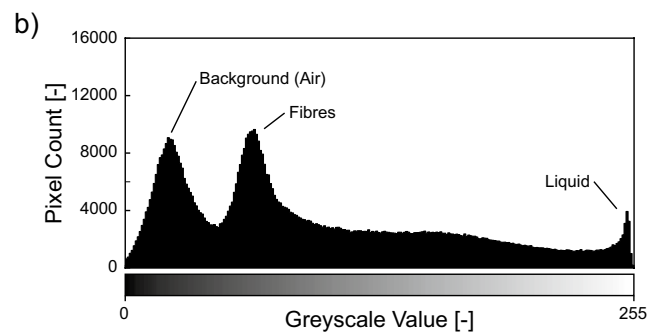
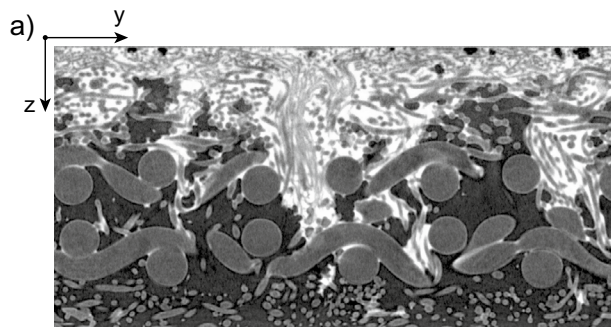


Fig. 8 μ CT scan of the underlying fabric for verification of the absorption contrast by using a concentration of 20% *KI* as the contrast agent in water. 40 μ l of liquid had been applied to a $D = 10$ mm sample **a** Greyscale tomography of the sample. Liquid, air and fibres

can clearly be distinguished by the eye. **b** Greyscale histogram of the tomography from (a). The liquid is responsible for the peak at high greyscale values

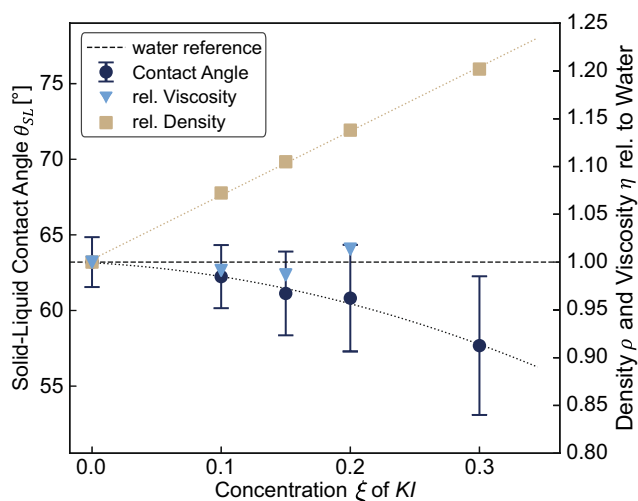


Fig. 9 Viscosity, density and solid–liquid contact angle of H₂O–KI solutions as a function of the KI concentration ξ . The bar at the contact angle measurements indicates the average standard deviation of the measurements

reference system is depicted in Fig. 6. A calculation of the absorption contrast on a virtual detector in yz-plane is possible using Beer–Lambert’s law (see Eq. 3) with the respective attenuation coefficients μ_{H_2O} , μ_{KI} and μ_{PA6} as listed in Table 2. The concentration of the contrast agent KI in water is defined as a mass ratio ξ :

$$\xi = \frac{m_{KI}}{m_{H_2O}} \tag{9}$$

To calculate the resulting attenuation coefficient of the liquid μ_L for different concentrations of KI, we consider the attenuation coefficients of the mass fractions w_i in the liquid:

$$w_{KI} = \frac{\xi}{1 + \xi} \tag{10}$$

$$\mu(w_{KI}) = w_{KI}\mu_{KI} + (1 - w_{KI})\mu_{H_2O} \tag{11}$$

The resulting absorption contrast on a detector in yz-plane can be seen in Fig. 7. While the absorption of the PA6 particles is always constant, the absorption of the surrounding liquid is increased, causing higher greyscale values that should allow to distinguish between the respective materials by greyscale thresholding. The simulation results reveal that starting at a KI concentration of around $\xi = 10\%$, the particles can be distinguished from the background with the bare eye. However, it is visible that using KI concentrations of $\xi > 20\%$, the particles can be separated from the background by greyscale contrast easily.

To verify these simulation results, we perform a μ CT scan of a partly saturated sample with a KI-concentration of $\xi = 20\%$ using beam parameters listed in Table 1 at a voxel size of 4 μ m. Figure 8a depicts the resulting greyscale tomography. As predicted by the simulation, a distinction between liquid, air and PA6 fibres should be possible. Analysing the greyscale histogram in Fig. 8b reveals that a third peak is visible at the highest greyscales, representing the liquid in the fibre network, allowing for a greyscale-based separation in liquid, air and the PA6 fibres.

However, the liquid distribution in partly saturated fibre networks is governed by Eqs. 2 and 3. By adding KI as a contrast agent, liquid properties like viscosity η , surface tension γ_{lg} , the solid–liquid contact angle θ_{sl} or density ρ can be significantly altered, which affects the liquid distribution (Mao and Russell 2003). As we aim to resolve the water distribution in partly saturated fibre networks, measuring and comparing these properties as a function of the concentration ξ is necessary to evaluate if the properties significantly differ from purified water. The viscosity was measured using a digital viscometer (Brookfield DV-I Prime, Brookfield Engineering Laboratories, INC. Middleboro, MA, USA). A determination of the density was possible using a measuring cylinder of 100 cm³ volume on a precision balance (XS4002, Mettler Toledo, Greifensee, Switzerland). A goniometer (PGX, Messmer Büchel, Veenendaal, Netherlands) was facilitated to measure the static contact angle against a solid PA6 surface that was cleaned after each measurement using isopropyl. As contact angle measurements usually scatter due to variations in the microstructure of the countersurface, these measurements are repeated ten times to calculate average data. All measurements have been conducted in an air-conditioned lab at 20°C. For better comparison of the results, the viscosity and density results are normalized to the measurement values of purified water.

As visible in Fig. 9, the density of the H₂O–KI solution increases linearly with 0.67% per % increase in the KI concentration ξ , which is a logical consequence as additional material is dissolved in the purified water. Increasing the KI concentration ξ does also not cause any significant changes in the viscosity measurements, as all measured values are within $\pm 1\%$ of the reference for purified water. The solid–liquid contact angle with PA6 is decreasing with a polynomial function of second order for increasing KI concentrations. As we know from the previous μ CT scan, $\xi < 20\%$ is sufficient to ensure a material separation. Therefore, the difference in contact angle is $\Delta\theta_{sl} < 4\%$ to the contact angle of purified water of $\theta_{sl} = 63.2^\circ$. Regarding the surface tension, we reconsider the definition of the static solid–liquid contact angle θ_{sl} :

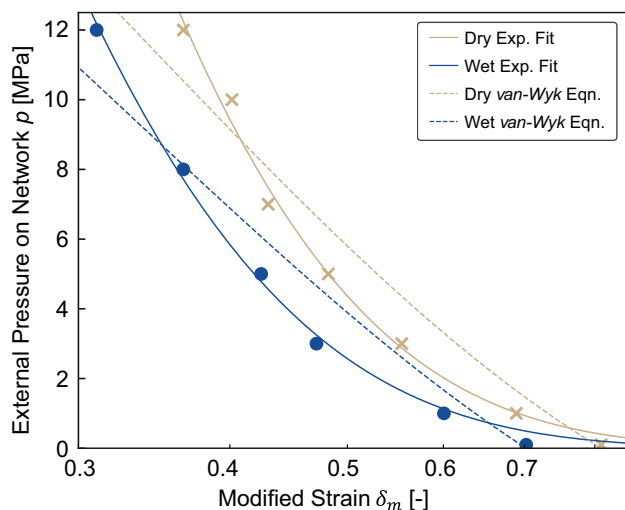


Fig. 10 Static compression properties of the dry and wet networks

$$\cos \theta_{sl} = \frac{\gamma_{sg} - \gamma_{sl}}{\gamma_{lg}} \tag{12}$$

Adding a contrast agent in the water does not influence the surface tension γ_{sg} . As the contact angle decreases by less than 4% with the necessary amount of contrast agent, we assume that also the surface tension γ_{lg} does not considerably differ from the value of purified water ($\gamma_{lg} = 72.8 \text{ mN/m}$). Therefore, we conclude that the relevant rheological properties are close enough to the rheological properties of purified water. Hence, *KI* can be used as a contrast agent at concentrations $\xi < 20\%$ without modifying the local distribution of water in the fibre network. However, using the minimum possible concentration is beneficial as this will

decrease the differences in liquid density and contact angle. As further μCT scans have shown, a *KI* concentration of $\xi = 12\%$ is sufficient for allowing a material distinction in the greyscale histogram. Therefore, the final scans in Sect. 3 are obtained using this concentration.

3 Results and discussion

As the here presented method has proven to differentiate between liquid, air and PA6 fibres within one tomographic scan, we study the water distribution of partly saturated fibre networks under external loads. Therefore, we apply $40 \mu\text{l}$ of 12% *KI* solution to the fabric described in Sect. 2 under a static load while performing a tomographic scan in a μCT using beam parameters as listed in Table 1. The loads were chosen to be 0.1, 1, 3, 5, 8 and 12 MPa. Scans conducted with 0.1 MPa loads induce a minimum of fibre alignment and are referred to as “unloaded”. Furthermore, dry scans of the loaded fibre network were also obtained for comparison to the compression properties of the wet fibre network.

3.1 Compression behaviour of the network in the partly saturated case

The static network compression properties in the dry and wet states are analysed to characterize the liquid redistribution under compression. The compression properties of fibre networks as a function of an external load p are often described using the equation derived by van Wyk (1946):

$$p = KE(v_f^3 - v_{f0}^3) \tag{13}$$

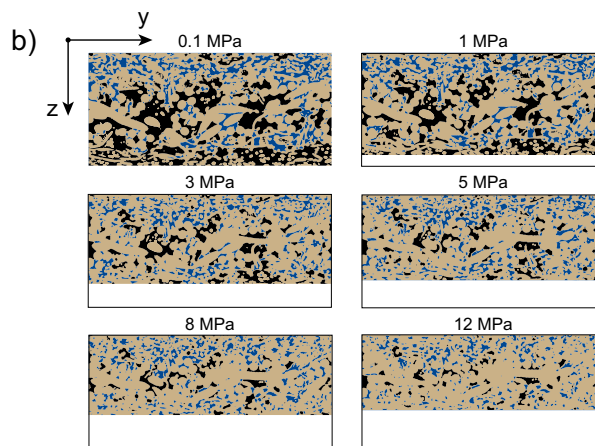
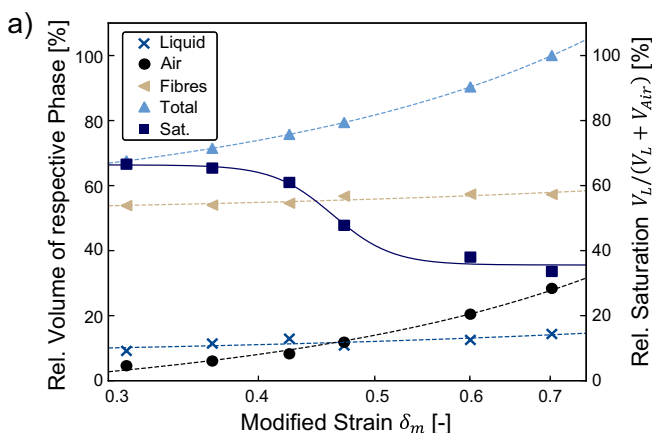


Fig. 11 Phase distribution and relative saturation of partly saturated fibre networks as a function of external load. **a** Relative phase volumes as a function of the applied load. Data are generated using voxel counting of the respective phases. **b** yz -plane view of the

microstructural distribution of the phases in the fibre network under applied load. Image height corresponds to the overall compression of the fibre network. Colour legend identical to part (a)

with the constant K , the elastic modulus of the fibre network E , the ratio of fibres in the network v_f under a given compression load p and the ratio of fibres in the network in the unloaded case v_{f0} . As fibre networks show high deformation under low loads, it is more convenient to use the modified strain δ_m to describe the respective compression state regarding the height of a poreless network h_0 :

$$\delta_m = \ln(h/h_0) \quad (14)$$

Using the correlation $v_f = 1/e^{\delta_m}$, van Wyk's equation (see Eq. 13) can be formulated as a function of the modified strain δ_m . The static compression properties of the dry and wet fibre networks are depicted in Fig. 10. Already at low external loads (0.1 MPa), significantly lower modified strains are visible for the wet fibre network ($\Delta\delta_m = 0.108$). This is attributed to capillary forces that deform the internal structure in the wet fibre network. Furthermore, the contacts between individual fibres are lubricated, causing the internal network friction to be lowered. This causes a lower threshold load p_t , which defines the load that needs to be exceeded before the deformation of the fibre network begins. As a result, the wet fibre network deforms already at lower external loads and reaches lower values of δ_m than the dry fibre network at equivalent external loads. Additionally, comparing the measured compression data to van Wyk's equation shows higher discrepancies. This is attributed to the simplifying assumptions in deriving van Wyk's equations, such as neglecting fibre twisting and friction between the fibres. Furthermore, the network does not show a random fibre orientation as assumed in van Wyk's equation but has a clear principal in-plane fibre direction in both the base and batt fibre layers. Even though there are extensions of van Wyk's models available that take into account fibre friction

(Beil and Roberts 2002; Beil et al. 2002), it is known that the pore volume decreases exponentially with increasing external pressure (Jaganathan et al. 2009). Hence, we are applying an exponential function of the kind:

$$p = a e^{(-b(\delta_m+c))} \quad (15)$$

to describe the compression properties of the fibre network using identical parameters a , b and c as a function of δ_m . As visible in Fig. 10, the function can describe the compression behaviour of the fibre networks with higher accuracy than van Wyk's model for external pressures of $p > 1$ MPa. A similarity in the compression behaviour between the dry and wet fabric is visible, even though the differences in the inter-fibre friction contact cause lower modified strains for the wet network.

3.2 Phase distribution under external compression of the medium

The phase distribution (liquid, fibres and air) as a function of the modified strain is analysed. This is done by evaluating the segmented scans and counting the voxel volumes assigned with the respective phase. As visible in Fig. 11a, the network is compressed by 67.7% of its original volume to $\delta_m = 0.310$ at the maximum load of 12 MPa. The decrease in air volume and total volume is nonlinear with increasing modified strain. It can be described using an exponential function of the kind:

$$V(p) = a e^p + b_i \quad (16)$$

with $a_{\text{Air}} = 0.376$, $b_{\text{Air}} = -0.480$, $a_{\text{Total}} = 0.496$ and $b_{\text{Total}} = -1.342 \cdot 10^{-9}$. The immediate decrease in air

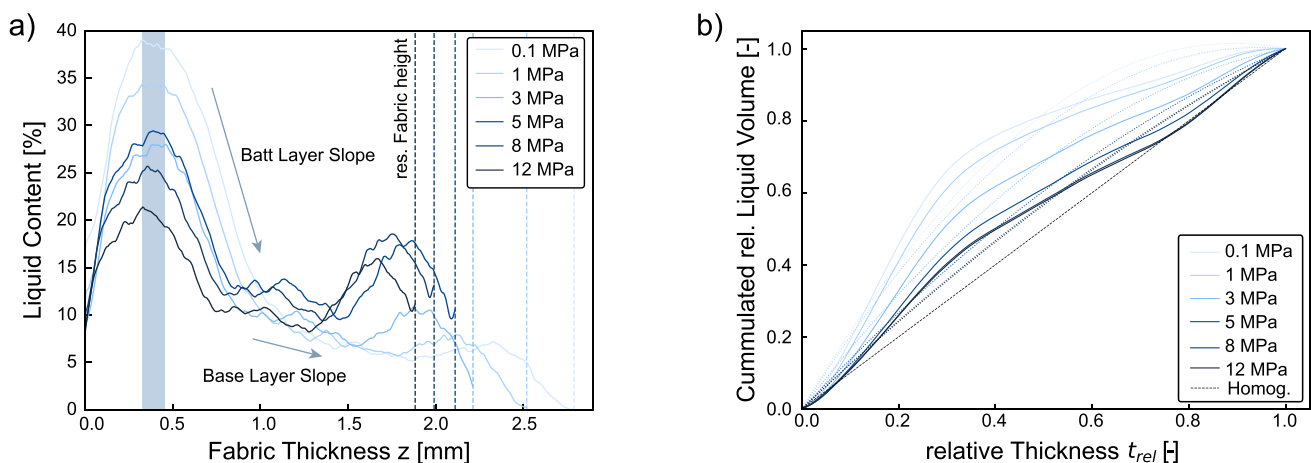


Fig. 12 Out-of-plane liquid distribution in the fibre network for increasing external loads. **a** Liquid content as a function of the fabric thickness. The decrease in fabric thickness with increasing external load is visible with the dashed line to denote the lower surface

position of the fibre network. **b** Accumulated liquid volume diagram of the z -directional liquid distribution for different external loads. Measured values are fitted with a polynomial function of second order (dotted curves)

content at low modified strains agrees with results from Centea and Hubert (2011) for carbon fibre-reinforced polymer composites. In contrast, the phase proportions of liquid and fibres are more or less constant. The 5.2% loss in the relative liquid volume is explained by an in-plane flow within the $D = 10$ mm sample out of the evaluated 6x6 mm domain. However, this is considered acceptable due to the generally low in-plane permeability of nonwoven fibre networks (Thibault et al. 2001). The compression, therefore, mainly causes the removal of air out of the fibre network, which confirms the hypothesis for the compression of partly saturated fibre networks (Vomhoff 1998; Wahlström 1969), stating that air inside wet paper networks is pressed out of the network at early stages of mechanical dewatering. However, even at an external load of 12 MPa, some air is still present within the fibre networks, causing a saturation content of 66.6%. By fitting a 4PL logistic function to the saturation data, one can also see that there will be a limiting saturation of around 67.2% for that specific initial water volume, even if the load is increased beyond 12 MPa. Consequently, air will always be present in the fabric regardless of the applied external load, assuming that the initial saturation is $<33.6\%$ and the fibres in the network are rigid, meaning that they do not deform under the applied load. Referring to the segmented 2D images depicted in Fig. 11b, the remaining air at higher loads acts as a barrier for the out-of-plane flow of water. Therefore, the resulting out-of-plane flow out of the fibre network is limited by unsaturated conditions. As a result, the dewatering of wet fibre networks might be enhanced by achieving saturated conditions, increasing their effective out-of-plane permeability. Furthermore, many

voids are still present in the base layer at 12 MPa, which is attributed to the relatively high compression stiffness of the woven structure compared to the nonwoven batt fibre layers. This limits the fabric's compressibility and offers many bigger pores that do not fill with liquid due to low capillary pressure. To achieve maximum fabric saturation, deformable base layers with small pore sizes should be facilitated in drainage applications.

3.3 z-directional liquid distribution in strained fibre networks

The liquid content in the fabric is analysed by counting the voxels assigned as liquid as a function of the fabric thickness (z) for different external loads. By evaluating the data visible in Fig. 12a, an inhomogeneous liquid distribution is present at 0.1 MPa with a peak of 39.0% at a depth of 0.33 mm below the top surface. This coincides with studies of the time-dependent oil distribution in nonwoven filters (Straube et al. 2023), where also the maximum liquid fraction was observed just below the top surface.

The liquid content then continuously decreases with increasing fabric thickness, as previously reported by Charvet et al. (2011). Two different characteristic slopes of the liquid distribution are visible for each compression state, which is attributed to the different pore sizes present in the batt fibre layer and base layer, respectively (see indications in Fig. 12). Just above the bottom surface, there is a local maximum in the liquid distribution, which can be explained by the back batt fibre layer. Liquid transported through the base layer in the fibre pillars will then accumulate in the back batt fibre layer

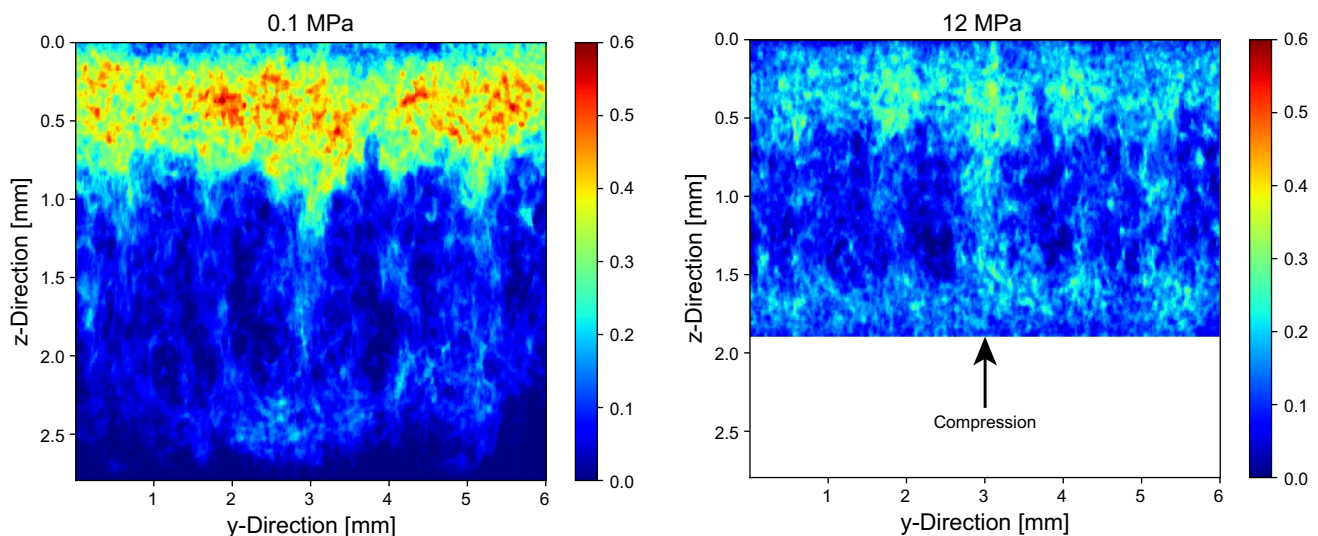


Fig. 13 2D projections of the out-of-plane liquid distribution in the yz -plane for the network at 0.1 and 12 MPa external load. Traces of liquid down into the backing batt fibre layer can be seen at 0.1 MPa,

while a homogenization of the liquid distribution takes place during compression to 12 MPa

once it reaches the locally small pores of the back batt fibre layer. Increasing the applied load makes a decrease in the overall maximum liquid content visible (down to 21.4% for 12 MPa). However, the location of these maxima is independent of the applied external load and is located 0.33–0.45 mm underneath the top surface. Furthermore, the second local maxima increases with the increase in external load. As the water content in the base layer (0.9–1.5 mm) increases, an out-of-plane flow is present that causes a redistribution of liquid towards the bottom batt fibre layer. This fosters a homogenization of the liquid distribution in the fibre network with increasing external load. The mentioned homogenization process with increasing external load can also be seen in the accumulated liquid volume diagram depicted in Fig. 12b. With increasing load, the overall curvatures of the graphs decreases and further aligns with the theoretical homogeneous distribution, which is a linear function in that case. Hence, the external load causes a redistribution of the liquid in the network, which fosters a homogeneous liquid distribution over the compressed fibre network's thickness. Active homogenization of liquid distribution with external loads could, therefore, be an effective countermeasure to an inhomogeneous accumulation of particles in the upper layers of nonwoven filters, as reported by Hoppe et al. (2022), Jackiewicz et al. (2015), and Riefler et al. (2018).

3.4 Influence of microstructural fabric design for the liquid distribution in strained fibre networks

To investigate the influence of the network's microstructure on the water distribution in the partly saturated case, voxels

classified as air and liquid are assigned with the respective material density. From this, it is possible to calculate the mean density along a principal direction (x,z), rendering the 2D liquid distribution across the fibre network projected on a specific plane (yz, xy). The out-of-plane liquid distributions (yz) for the cases of 0.1 and 12 MPa are depicted in Fig. 13 (see Appendix A for all load steps). At a load of 0.1 MPa, the liquid accumulates in the upper batt fibre layers 1 and 2, and an immediate decrease in saturation at the base fibre layer is visible, similar as reported by Chaudhuri et al. (2022). This is explained by high capillary forces resulting from the small pore sizes in the upper batt fibre layers. Furthermore, traces of liquid penetrating the base layer into the back batt fibre layer can be seen. This is explained with local fibre pillars resulting from the punch-needling process used in manufacturing the nonwoven structure. This process causes fibres from the upper batt layers to be punched down into the base layer of the network, forming local areas of small pore sizes in the base layer. This causes locally high capillary forces, which transport liquid along the fibre pillars. Hence, the intensity of this punch-needling process significantly enhances the out-of-plane liquid transport through the base layer. The transport of liquid along the fibre pillars in the z -direction can also be explained by the capillary phenomenon occurring only along the fibre orientation (Mao and Russell 2003). Within the fibre pillars, the nonwoven fibres are also oriented in z -direction (Jaganathan et al. 2009), causing a more accessible transport of liquid down along the fibre orientation. It is also visible that big pores in the base layer of the network act as barriers for out-of-plane liquid transport as they do not collapse even at higher external loads. Therefore, hierarchical fibre networks can

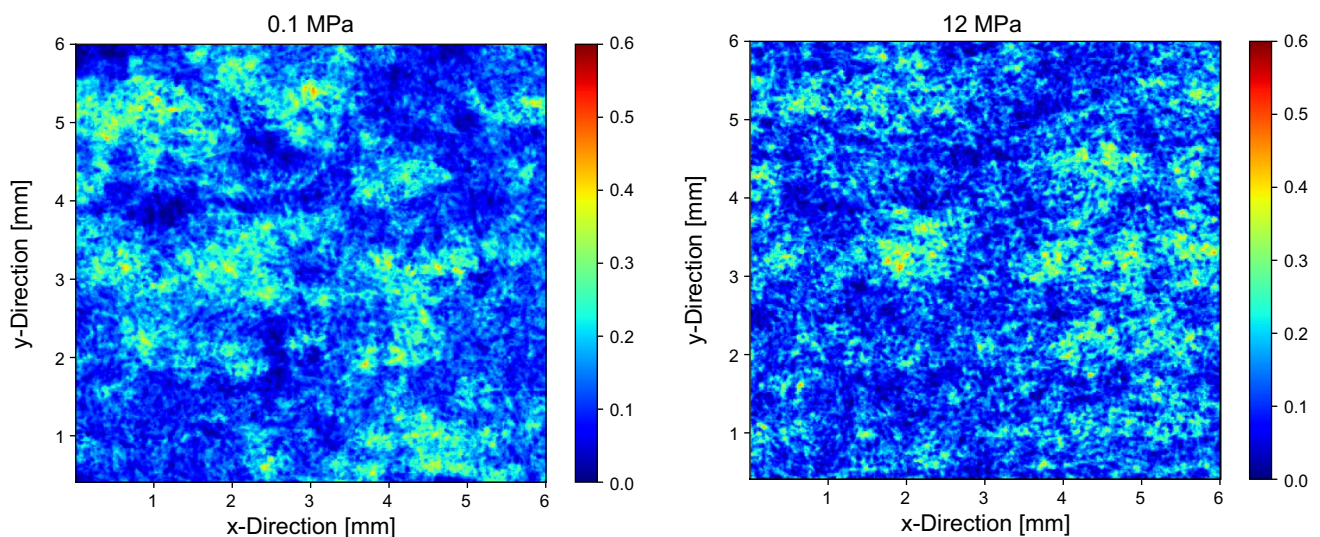


Fig. 14 2D projections of the in-plane liquid distribution in the xy -plane for the network at 0.1 and 12 MPa external load. Accumulations of liquid are still visible at fibre pillars even at 12 MPa

show a significant anisotropy in permeability, supported by earlier observations by Thibault et al. (2001).

As depicted in Fig. 13, an increase in the external loads acting on the network causes homogenization of the out-of-plane liquid distribution, which aligns with previous studies for woven networks (Rossi et al. 2011; Stämpfli et al. 2013). The liquid is transported from the areas of high saturation in the upper batt layer through the fibre pillars down into the backing batt fibre layer, where it accumulates. Hence, the homogenization of the liquid distribution seen in Sect. 3.3 can be described with the microstructure of the network. However, some areas in the base layer still do not collapse at the 12 MPa external load, creating a low local capillary pressure resulting in a low local saturation. Besides the out-of-plane liquid distribution, the in-plane liquid distribution is investigated using the projections shown in Fig. 14 (see Appendix B for all load steps). For the unloaded case, it is visible that an inhomogeneous liquid distribution is also present, even though it is less pronounced. In contrast to the out-of-plane case, the liquid distribution does not significantly homogenize during the compression process. Hence, for the 12 MPa projection, there are still areas with high saturation visible. This can be explained by the fact that the liquid captured in the small pores of the fibre pillars will not be pressed into the coarse pores in the surrounding base layer. Hence, a principal inhomogeneous distribution will be present even at a higher compression state, which is somehow limited by the occurring in-plane flow once the liquid has reached the backing batt fibre layer. Furthermore, the liquid might also be transported in-plane along the base layer in the meniscus that forms between two twisted fibres, following the observations of Leisen and Beckham (2008) for wet woven fibre networks.

4 Conclusion

Within our study, we developed a novel method to resolve the liquid distribution in partly saturated nonwoven fibre networks on the microscale using tomographic imaging. The key challenge of sufficient attenuation contrast between the PA6 fibres and the liquid was solved using a solution of 12% KI in water, which increases the resulting attenuation coefficient of the liquid to a certain level, allowing for phase segmentation based on the greyscales in the tomographic images. The found contrast liquid is also beneficial, as it maintains the rheological properties of purified water, allowing for a comparison of the results with the behaviour of purified water in a partly saturated PA6 fibre network. By applying the method to a fibre network consisting of nonwoven batt layers needle punched on a woven base layer, we could investigate the influence of the network's microstructure on the resulting liquid distribution under

partly saturated conditions. As this is a direct consequence of the fibre network design, our novel method allows us to investigate its influence on the final product performance. By applying a static external load, we also deformed the fibre network's microstructure and noticed an increasing homogenization of the out-of-plane liquid distribution, which could be beneficial for extending the lifetime of filters as the liquid can be transported in originally unsaturated areas. Also, we noticed that the needle-punching process of the nonwoven network created fibre pillars, which considerably influenced the liquid distribution in the partly saturated case. Therefore, this manufacturing step could modify the out-of-plane liquid distribution in the fibre network, allowing for customizing the material for specific applications by adjusting the needle punching process. As a result, this method is an essential tool for creating novel fibre network designs that show superior liquid distribution and permeability, allowing for optimized drainage process conditions for a sustainable future. Besides the static investigation, time-resolved tomographic measurements of the dynamic liquid spread in nonwoven networks would further increase the understanding of liquid spread, generating a comprehensive view of the liquid distribution in nonwoven fibre networks. However, due to the need for sample rotation in tomographic imaging, centrifugal forces might alter the results, limiting a possible temporal resolution. Therefore, the novel developed X-ray multiprojection (XMPI) technology (Villanueva-Perez et al. 2018) could be a possible solution, allowing for a time-resolved study of flow systems without requiring a sample rotation. However, X-ray-based methods can only expose a comparatively small volume of the overall fabric. As interactions of the fabric with itself and inhomogeneities induced in fabric during the manufacturing process will significantly adapt the final fabric performance, it seems beneficial to perform several scans with multiple specimens from the same fabric sample to generate average data. This should allow to get an idea about the fabric behaviour on the macroscale by evaluating the data on the microscale.

Appendix A. Out-of-plane liquid distribution projected on yz-plane

See Fig. 15.

Appendix B. In-plane liquid distribution projected on xy-plane

See Fig. 16.

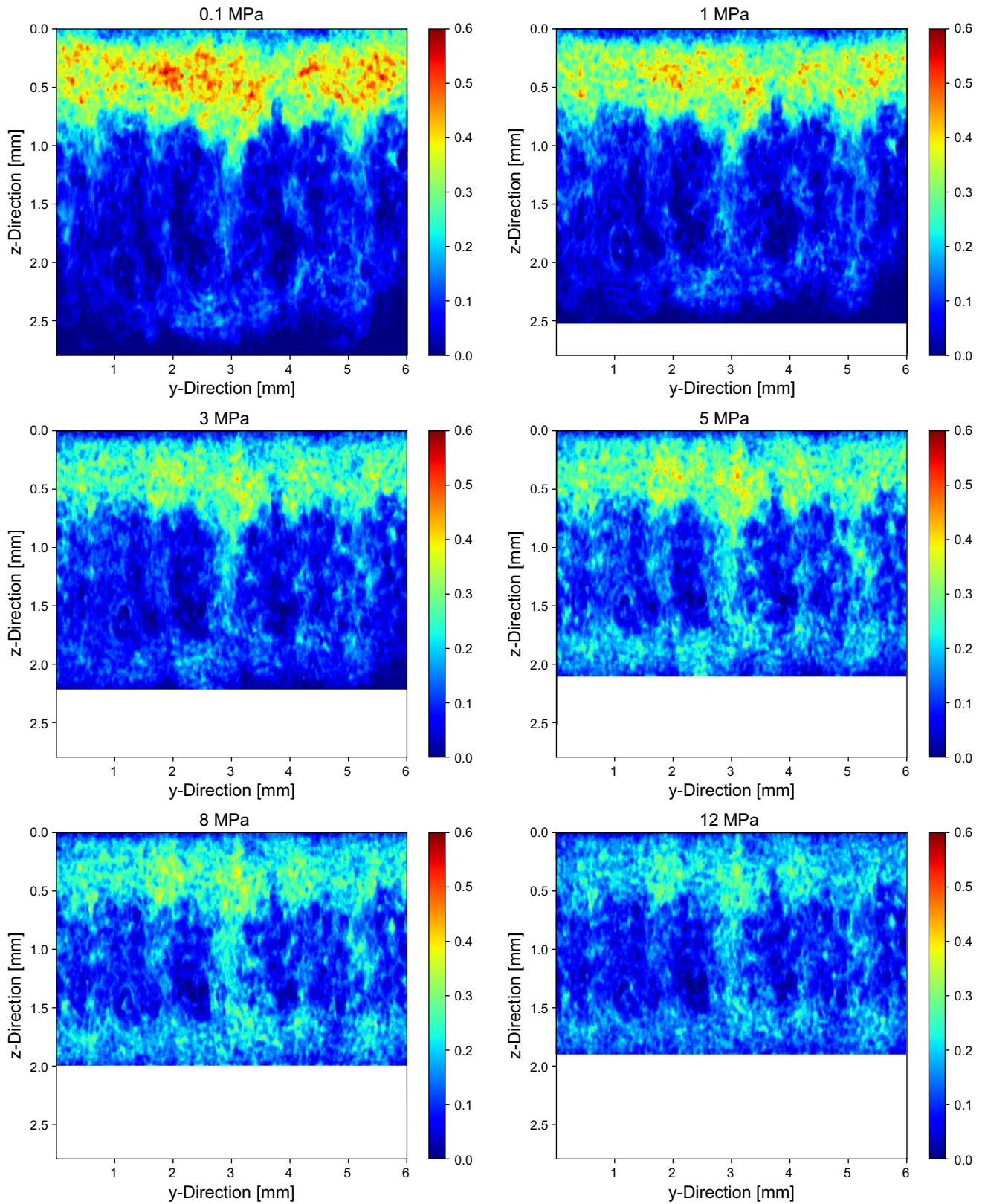


Fig. 15 Out-of-plane liquid distribution in the fibre network for increasing external loads. Projection of average density of liquid projected on yz -plane. Network height (z) is decreasing with increasing load

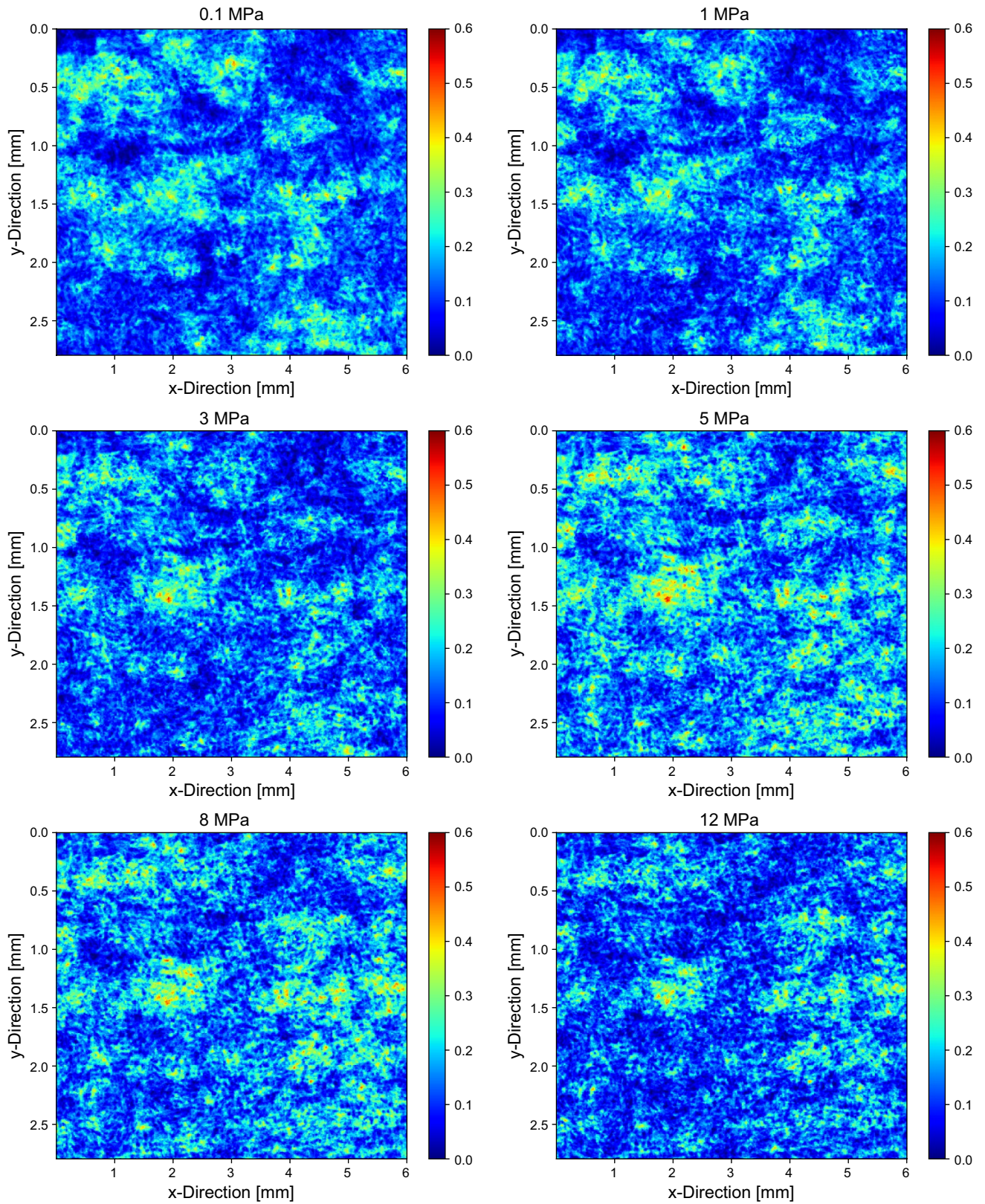


Fig. 16 In-plane liquid distribution in the fibre network for increasing external loads. Projection of average density of liquid projected on xy -plane. Decrease in network height (z) not visible due to projection

Acknowledgements The authors greatly acknowledge the support of Richard Westerholz in performing the underlying tomographic scans. Julia Katharina Rogalinski is thanked for her support with the PA6 attenuation calculations. The Knut and Alice Wallenberg Foundation is acknowledged for the funding of Daniel Söderberg through the Wallenberg Wood Science Center.

Author contributions Conceptualisation, methodology, data collection, investigation, visualization, writing, and revising the original draft were done by PW. Methodology (supporting), investigation (supporting) and revising the original draft were done by TR. Conceptualisation, review and editing, and supervision were done by DS.

Funding Open access funding provided by Royal Institute of Technology.

Data availability The data that support the findings of this study are available upon reasonable request from the authors.

Declarations

Conflict of interest Patrick Wegele reports financial support and equipment were provided by J.M. Voith SE & Co. KG. Patrick Wegele reports a relationship with J.M. Voith SE & Co. KG, including employment. The other authors declare that they have no conflict of interest.

Ethical approval Not applicable.

Open Access This article is licensed under a Creative Commons Attribution 4.0 International License, which permits use, sharing, adaptation, distribution and reproduction in any medium or format, as long as you give appropriate credit to the original author(s) and the source, provide a link to the Creative Commons licence, and indicate if changes were made. The images or other third party material in this article are included in the article's Creative Commons licence, unless indicated otherwise in a credit line to the material. If material is not included in the article's Creative Commons licence and your intended use is not permitted by statutory regulation or exceeds the permitted use, you will need to obtain permission directly from the copyright holder. To view a copy of this licence, visit <http://creativecommons.org/licenses/by/4.0/>.

References

- Beil NB, Roberts WW (2002) Modeling and computer simulation of the compressional behavior of fiber assemblies: part II: hysteresis, crimp, and orientation effects. *Text Res J* 72(5):375–382. <https://doi.org/10.1177/004051750207200501>
- Beil NB, William W, Roberts J (2002) Modeling and computer simulation of the compressional behavior of fiber assemblies: part I: comparison to van wyk's theory. *Text Res J* 72(4):341–351. <https://doi.org/10.1177/004051750207200411>
- Bencsik M, Adriaansen H, Brewer SA, McHale G (2008) Quantitative NMR monitoring of liquid ingress into repellent heterogeneous layered fabrics. *J Magn Reson* 193(1):32–36. <https://doi.org/10.1016/j.jmr.2008.04.003>
- Biguenet F, Stämpfli R, Krügl S, Georges T, Dupuis D, Rossi RM, Bueno M-A (2024) Forced wetting of hydrophobic knitted fabrics analyzed with x-ray imaging. *Text Res J* 94(1–2):90–107. <https://doi.org/10.1177/00405175231201168>
- Birrfelder P, Dorrestijn M, Roth C, Rossi RM (2013) Effect of fiber count and knit structure on intra- and inter-yarn transport of liquid water. *Text Res J* 83(14):1477–1488. <https://doi.org/10.1177/0040517512460296>
- Carrel M, Beltran MA, Morales VL, Derlon N, Morgenroth E, Kaufmann R, Holzner M (2017) Biofilm imaging in porous media by laboratory x-ray tomography: combining a non-destructive contrast agent with propagation-based phase-contrast imaging tools. *PLoS ONE*. <https://doi.org/10.1371/journal.pone.0180374>
- Centea T, Hubert P (2011) Measuring the impregnation of an out-of-autoclave prepreg by micro-CT. *Compos Sci Technol* 71(5):593–599. <https://doi.org/10.1016/j.compscitech.2010.12.009>
- Charvet A, Roscoat Rolland DS, Peralba M, Bloch J, Gonthier Y (2011) Contribution of synchrotron x-ray holotomography to the understanding of liquid distribution in a medium during liquid aerosol filtration. *Chem Eng Sci* 66(4):624–631. <https://doi.org/10.1016/j.ces.2010.11.008>
- Chaudhuri J, Boettcher K, Ehrhard P (2022) Optical investigations into wetted commercial coalescence filter using 3D micro-computer-tomography. *Chem Eng Sci*. <https://doi.org/10.1016/j.ces.2021.117096>
- Davit Y, Iltis G, Debenest G, Veran-Tissoires S, Wildenschild D, Gerino M, Quintard M (2011) Imaging biofilm in porous media using x-ray computed microtomography. *J Microsc* 242(1):15–25. <https://doi.org/10.1111/j.1365-2818.2010.03432.x>
- Eller J, Rosén T, Marone F, Stampanoni M, Wokaun A, Bchi FN (2011) Progress in in situ x-ray tomographic microscopy of liquid water in gas diffusion layers of PEFC. *J Electrochem Soc* 158(8):963–970. <https://doi.org/10.1149/1.3596556>
- Endruweit A, Glover P, Head K, Long AC (2011) Mapping of the fluid distribution in impregnated reinforcement textiles using magnetic resonance imaging: methods and issues. *Compos A* 42(3):265–273. <https://doi.org/10.1016/j.compositesa.2010.11.012>
- Feldkamp LA, Davis LC, Kress JW (1984) Practical cone-beam algorithm. *J Opt Soc Am A* 1(6):612–619. <https://doi.org/10.1364/JOSAA.1.000612>
- Ferdoush S, Kzam SB, Martins PH, Dewancke J, Gonzalez M (2023) Fast time-resolved micro-CT imaging of pharmaceutical tablets: insights into water uptake and disintegration. *Int J Pharm*. <https://doi.org/10.1016/j.ijpharm.2023.123565>
- Gupta GS, Litster JD, Rudolph VR, White ET (1997) Flow visualisation study in porous media using x-rays. *Steel Res* 68(10):434–440. <https://doi.org/10.1002/srin.199700579>
- Halls B, Gord J, Schultz L, Slowman W, Lightfoot M, Roy S, Meyer T (2018) Quantitative 10–50 KHZ x-ray radiography of liquid spray distributions using a rotating-anode tube source. *Int J Multiph Flow*. <https://doi.org/10.1016/j.ijmultiphaseflow.2018.07.014>
- Harnett P, Mehta P (1984) A survey and comparison of laboratory test methods for measuring wicking. *Text Res J* 54(7):471–478. <https://doi.org/10.1177/004051758405400710>
- Henke B, Gullikson E, Davis J (1993) X-ray interactions: photoabsorption, scattering, transmission, and reflection at $e = 50\text{--}30,000\text{ eV}$, $z = 1\text{--}92$. *At Data Nucl Data Tables* 54(2):181–342. <https://doi.org/10.1006/adnd.1993.1013>
- Hilpert M, Miller CT (2001) Pore-morphology-based simulation of drainage in totally wetting porous media. *Adv Water Resour* 24(3):243–255. [https://doi.org/10.1016/S0309-1708\(00\)00056-7](https://doi.org/10.1016/S0309-1708(00)00056-7)
- Hobisch MA, Zabler S, Bardet SM, Zankel A, Nypelö T, Eckhart R, Bauer W, Spirk S (2021) How cellulose nanofibrils and cellulose microparticles impact paper strength—a visualization approach. *Carbohydr Polym*. <https://doi.org/10.1016/j.carbpol.2020.117406>
- Hollies NRS, Kaessinger MM, Watson BS, Bogaty H (1957) Water transport mechanisms in textile materials: part II: capillary-type

- penetration in yarns and fabrics. *Text Res J* 27(1):8–13. <https://doi.org/10.1177/004051755702700102>
- Hoppe K, Schaldach G, Zielke R, Tillmann W, Thommes M, Pieloth D (2022) Experimental analysis of particle deposition in fibrous depth filters during gas cleaning using x-ray microscopy. *Aerosol Sci Technol* 56(12):1114–1131. <https://doi.org/10.1080/02786826.2022.2132133>
- Hu J, Li Y, Yeung K-W, Wong ASW, Xu W (2005) Moisture management tester: a method to characterize fabric liquid moisture management properties. *Text Res J* 75(1):57–62. <https://doi.org/10.1177/004051750507500111>
- Hyvälouma J, Raiskinmäki P, Jäsberg A, Koponen A, Kataja M, Timonen J (2006) Simulation of liquid penetration in paper. *Phys Rev E Stat Nonlinear Soft Matter Phys.* <https://doi.org/10.1103/PhysRevE.73.036705>
- Iltis GC, Armstrong RT, Jansik DP, Wood BD, Wildenschild D (2011) Imaging biofilm architecture within porous media using synchrotron-based x-ray computed microtomography. *Water Resour Res.* <https://doi.org/10.1029/2010WR009410>
- Ivankovic T, Rolland du Roscoat S, Geindreau C, Séchet P, Huang Z, Martins JMF (2016) Development and evaluation of an experimental protocol for 3-D visualization and characterization of the structure of bacterial biofilms in porous media using laboratory x-ray tomography. *Biofouling* 32(10):1235–1244. <https://doi.org/10.1080/08927014.2016.1249865>
- Jackiewicz A, Jakubiak S, Gradoń L (2015) Analysis of the behavior of deposits in fibrous filters during non-steady state filtration using x-ray computed tomography. *Sep Purif Technol.* <https://doi.org/10.1016/j.seppur.2015.10.004>
- Jaganathan S, Vahedi Tafreshi H, Shim E, Pourdeyhimi B (2009) A study on compression-induced morphological changes of nonwoven fibrous materials. *Colloids Surf A* 337(1):173–179. <https://doi.org/10.1016/j.colsurfa.2008.12.019>
- Leisen J, Beckham H (2008) Void structure in textiles by nuclear magnetic resonance. part I. Imaging of imbibed fluids and image analysis by calculation of fluid density autocorrelation functions. *J Text Inst* 99(3):243–251. <https://doi.org/10.1080/00405000701404122>
- Leisen J, Beckham HW (2001) Quantitative magnetic resonance imaging of fluid distribution and movement in textiles. *Text Res J* 71(12):1033–1045. <https://doi.org/10.1177/004051750107101201>
- Manke I, Hartnig C, Grünerbel M, Lehnert W, Kardjilov N, Haibel A, Banhart J, Riesemeier H (2007) Investigation of water evolution and transport in fuel cells with high resolution synchrotron x-ray radiography. *Appl Phys Lett* 90(17):174105. <https://doi.org/10.1063/1.2731440>
- Mao N, Russell SJ (2003) Anisotropic liquid absorption in homogeneous two-dimensional nonwoven structures. *J Appl Phys* 94(6):4135–4138. <https://doi.org/10.1063/1.1598627>
- Markicevic B, Navaz H (2009) Numerical solution of wetting fluid spread into porous media. *Int J Numer Methods Heat Fluid Flow* 19(3–4):521–534. <https://doi.org/10.1108/09615530910938416>
- Penner T, Meyer J, Dittler A (2021) Characterization of mesoscale inhomogeneity in nonwovens and its relevance in the filtration of fine mists. *J Aerosol Sci.* <https://doi.org/10.1016/j.jaerosci.2020.105674>
- Riefler N, Ulrich M, Morshäuser M, Fritsching U (2018) Particle penetration in fiber filters. *Particuology.* <https://doi.org/10.1016/j.partic.2017.11.008>
- Roels S, Carmeliet J (2006) Analysis of moisture flow in porous materials using microfocus x-ray radiography. *Int J Heat Mass Transf* 49(25):4762–4772. <https://doi.org/10.1016/j.ijheatmasstransfer.2006.06.035>
- Rossi RM, Stämpfli R, Psikuta A, Rechsteiner I, Brühwiler PA (2011) Transplanar and in-plane wicking effects in sock materials under pressure. *Text Res J* 81(15):1549–1558. <https://doi.org/10.1177/0040517511413317>
- Russell SJ (2022) *Handbook of nonwovens*, 2nd edn. Elsevier, Cambridge
- Schulz VP, Becker J, Wiegmann A, Mukherjee PP, Wang C-Y (2007) Modeling of two-phase behavior in the gas diffusion medium of PEFCs via full morphology approach. *J Electrochem Soc* 154(4):B419. <https://doi.org/10.1149/1.2472547>
- Straube C, Meyer J, Dittler A (2023) Investigation of the local oil distribution on oleophilic mist filters applying x-ray micro-computed tomography. *Sep Purif Technol.* <https://doi.org/10.1016/j.seppur.2023.123279>
- Stämpfli R, Brühwiler PA, Rechsteiner I, Meyer VR, Rossi RM (2013) X-ray tomographic investigation of water distribution in textiles under compression-possibilities for data presentation. *Measurement* 46(3):1212–1219. <https://doi.org/10.1016/j.measurement.2012.11.009>
- Thibault X, Bloch J-F (2002) Structural analysis by x-ray microtomography of a strained nonwoven papermaker felt. *Text Res J* 72(6):480–485. <https://doi.org/10.1177/004051750207200603>
- Thibault X, Chave Y, Serra-Tosio J, Bloch J (2001) Permeability measurements of press felts. In: *The science of papermaking-12th fundamental research symposium*, vol 2, pp 947–974
- Van Langenhove L, Kiekens P (2001) Textiles and the transport of moisture. *Text Asia* 32(2):32–34
- van Wyk CM (1946) Note on the compressibility of wool. *J Text Inst Trans* 37(12):285–292. <https://doi.org/10.1080/19447024608659279>
- Villanueva-Perez P, Pedrini B, Mokso R, Vagovic P, Guzenko VA, Leake SJ, Willmott PR, Oberta P, David C, Chapman HN, Stapanoni M (2018) Hard x-ray multi-projection imaging for single-shot approaches. *Optica* 5(12):1521–1524. <https://doi.org/10.1364/OPTICA.5.001521>
- Vomhoff H (1998) Dynamic compressibility of water-saturated fibre networks and influence of local stress variations in wet pressing. *StockholmDiss (sammanfattning)*. Dissertation, KTH Royal Institute of Technology Stockholm
- Wahlström P (1969) Our present understanding of the fundamentals of pressing. *Pulp Pap Mag Can* 70:76–96
- Wallmeier M, Barbier C, Beckmann F, Brandberg A, Holmqvist C, Kulachenko A, Moosmann J, Ostlund S, Pettersson T (2021) Phenomenological analysis of constrained in-plane compression of paperboard using micro-computed tomography imaging. *Nord Pulp Pap Res J* 36(3):491–502. <https://doi.org/10.1515/npprj-2020-0092>
- Washburn EW (1921) The dynamics of capillary flow. *Phys Rev.* <https://doi.org/10.1103/PhysRev.17.273>
- Weder M, Brühwiler PA, Laib A (2006) X-ray tomography measurements of the moisture distribution in multilayered clothing systems. *Text Res J* 76(1):18–26. <https://doi.org/10.1177/0040517506053910>
- Yamaguchi S, Kato S, Kato A, Matsuoka Y, Nagai Y, Suzuki T (2021) Visualization of dynamic behavior of liquid water in the microporous layer of polymer electrolyte fuel cell during water injection by time-resolved x-ray computed tomography. *Electrochem Commun.* <https://doi.org/10.1016/j.elecom.2021.107059>
- Yousefi B, Varkiani SMH, Saharkhiz S, Toussi ZK (2021) The effect of inner layer fiber diameter and fabric structure on transplanar water absorption and transfer of double-layered knitted fabrics. *Fibers Polym* 22(2):578–586. <https://doi.org/10.1007/s12221-021-9430-5>
- Zhang G, Parwani R, Stone CA, Barber AH, Botto L (2017) X-ray imaging of transplanar liquid transport mechanisms in single layer

textiles. *Langmuir* 33(43):12072–12079. <https://doi.org/10.1021/acs.langmuir.7b02982>

Zhang G, Zhang Q (2022) Digital imaging of the oil permeation mechanism in an oleophobic textile. *Text Res J* 92(15–16):2662–2668. <https://doi.org/10.1177/00405175211006944>

Zhuang Q, Harlock S, Brook D (2002) Transfer wicking mechanisms of knitted fabrics used as undergarments for outdoor activities.

Text Res J 72(8):727–734. <https://doi.org/10.1177/004051750207200813>

Publisher's Note Springer Nature remains neutral with regard to jurisdictional claims in published maps and institutional affiliations.